



Cite this: *RSC Appl. Interfaces*, 2025, 2, 1650

## Interface magnetism in vanadium-doped MoS<sub>2</sub>/graphene heterostructures

Diem Thi-Xuan Dang,<sup>iD</sup><sup>a</sup> Yen Thi-Hai Pham,<sup>iD</sup><sup>a</sup> Da Zhou,<sup>iD</sup><sup>bc</sup> Dai-Nam Le,<sup>iD</sup><sup>a</sup> Mauricio Terrones,<sup>iD</sup><sup>bc</sup> Manh-Huong Phan<sup>iD</sup><sup>\*a</sup> and Lilia M. Woods<sup>iD</sup><sup>\*a</sup>

Magnetism in two-dimensional materials is of great importance in discovering new physical phenomena and developing new devices at the nanoscale. In this paper, first-principles simulations are used to calculate the electronic and magnetic properties of heterostructures composed of graphene and MoS<sub>2</sub> considering the influence of point defects and vanadium doping. It is found that the concentration of the dopants and the types of defects can result in induced magnetic moments leading to ferromagnetically polarized systems with sharp interfaces. This provides a framework for interpreting the experimental observations of enhanced ferromagnetism in both MoS<sub>2</sub>/graphene and V-doped MoS<sub>2</sub>/graphene heterostructures. The computed electronic and spin polarizations give a microscopic understanding of the origin of ferromagnetism in these systems and illustrate how doping and defect engineering can lead to targeted property tunability. Our work has demonstrated that through defects engineering, ferromagnetism can be achieved in V-doped MoS<sub>2</sub>/graphene heterostructures, providing a potential way to induce magnetization in other TMDC/graphene materials and opening new opportunities for their applications in nano-spintronics.

Received 15th April 2025,  
Accepted 30th July 2025

DOI: 10.1039/d5lf00113g

rsc.li/RSCApplInter

### 1 Introduction

The properties of low-dimensional materials and heterostructures (HSTs), in which relatively weak dispersion interactions play an important role, are strongly modified by the proximity effect. A prominent example is graphene, which experiences relatively strong proximity spin-orbit coupling (SOC) effects when placed on transition metal dichalcogenides (TMDC). Low-dimensional HSTs are currently used in optospintronics,<sup>1,2</sup> as well as in a variety of applications where the spin Hall effect and the spin galvanic effect are prominent.<sup>3,4</sup>

Typically, TMDC/graphene HSTs are non-magnetic. Nevertheless, the development of methods to effectively generate and control magnetism in 2D materials is critical for the establishment of new magnetic HSTs with various applications. An effective method to induce magnetic properties in 2D semiconductors involves doping and defect engineering.<sup>5,6</sup> Based on previous studies, transition metal substitutional doping can

effectively generate tunable magnetism in TMDC systems.<sup>7,8</sup> Among them, Vanadium doping can realize not only p-type transport behavior in TMDCs but also room-temperature ferromagnetism, making V-doped TMDCs a favorable platform for electronic and spintronic devices.<sup>9,10</sup>

Recently, V-doped MoS<sub>2</sub> has been intensively studied. Zhang *et al.* demonstrated that V-doped MoS<sub>2</sub> increases radiative recombination of excitons relative to trions by reducing background electrons in MoS<sub>2</sub>.<sup>11</sup> Sahoo *et al.* reported the presence of time-reversal asymmetry between the two *K*-valleys with a 32 meV relative energy shift between them.<sup>12</sup> Maity *et al.* observed a semiconductor-to-metal transition in V-doped MoS<sub>2</sub> alloy when the doping concentration increased above 5%.<sup>13</sup> The magnetic performance of the V-doped MoS<sub>2</sub> can be tuned by varying the doping concentration. In particular, enhanced ferromagnetism is observed for up to 3% V doping concentration,<sup>14</sup> which is strongly inhibited by raising doping beyond 8%.<sup>14</sup> However, due to the low doping concentration, the net magnetization of these monolayers remains relatively weak limiting their suitability for spintronic and magnetic sensor applications.

Constructing a HST of a doped TMDC exhibiting ferromagnetic behavior and a nonmagnetic 2D system such as graphene brings forward new possibilities for magnetic HSTs with sharp interfaces. Of special interest is to see if graphene can become magnetic as a result of interactions and proximity effects with the ferromagnetic TMDC.<sup>15,16</sup> In

<sup>a</sup> Department of Physics, University of South Florida, Tampa, Florida 33620, USA.  
E-mail: phanm@usf.edu, lmwoods@usf.edu

<sup>b</sup> Department of Physics, The Pennsylvania State University, University Park, Pennsylvania 16802, USA

<sup>c</sup> Center for 2-Dimensional and Layered Materials, The Pennsylvania State University, University Park, Pennsylvania 16802, USA

<sup>\*</sup> Current address: Department of Physics and Astronomy, George Mason University, Fairfax, Virginia 22030, USA.



this study, we broaden our understanding of doped TMDCs and their magnetism by investigating V-doped  $\text{MoS}_2$ /graphene HSTs by taking into account various types of defects and doping concentrations. In graphene, mono- and divacancies, Stone–Wales defects, *etc.* have been studied quite extensively.<sup>17,18</sup> The fabrication of TMDCs can also result in various types of vacancies,<sup>19,20</sup> including V-doped  $\text{MoS}_2$  monolayer obtained by chemical vapor deposition methods.<sup>14</sup> These vacancies are known to have dramatic effects on the electronic, magnetic, and optical properties of TMDC systems.<sup>14,21,22</sup> Due to their importance, in this paper, we have systematically studied the role of point defects in the properties of the V-doped  $\text{MoS}_2$ /graphene HST. We present various types of defect formations, the electronic structures of the defective materials, and the defect signatures of the magnetic properties of the different HSTs. Our work shows pathways to improve the saturation magnetization of TMDC/graphene HSTs, which can be useful for their application in spintronics.

## 2 Results and discussions

### 2.1 Structural properties

The primary investigation system is a HST formed by stacking a single graphene layer (Gr) and a single  $\text{MoS}_2$  layer. To initiate the calculations, we construct an atomistic supercell consisting of 162 C atoms ( $9 \times 9 \times 1$  Gr unit cell) and 49 Mo, 98 S atoms ( $7 \times 7 \times 1$   $\text{MoS}_2$  unit cell). After relaxation, the in-plane lattice constant of the Gr/ $\text{MoS}_2$  HST is  $a = b = 22.183 \text{ \AA}$ . As a reference, each monolayer is also simulated separately with an optimized lattice constant for Gr found as  $a = b = 2.471 \text{ \AA}$ , while the optimized lattice constant for  $\text{MoS}_2$  is  $a = b = 3.153 \text{ \AA}$ .

In addition to a HST composed of pristine monolayers, several point-like defects in both monolayers are considered, because isolated point defects are unavoidable in the synthesis process as discussed earlier. Specifically, a C monovacancy (Gr +  $\text{V}_\text{C}$ ), C divacancies (Gr +  $\text{V}_{2\text{C}}$ ) and Stone–Wales (Gr +  $\text{V}_{\text{SW}}$ ) defect

are constructed in the Gr part of the supercell. The defective TMDC monolayers are also generated in the  $\text{MoS}_2$  part of the supercell and they are:  $\text{MoS}_2 + \text{V}_\text{S}$  (with a S monovacancy),  $\text{MoS}_2 + \text{V}_{\text{S-S}}$  (with two adjacent S vacancies on the same S layer),  $\text{MoS}_2 + \text{V}_{2\text{S}}$  (with two S vacancies on the same Mo atom but in opposite S layers),  $\text{MoS}_2 + \text{V}_\text{Mo}$  (with a Mo monovacancy) and  $\text{MoS}_2 + \text{V}_{\text{Mo+2S}}$  (with a Mo vacancy and two S vacancies on opposite layers). To probe the magnetism in the system, Vanadium substitutional dopants at the Mo sites in the TMDC layer are simulated by taking  $\text{V}_{0.02}\text{Mo}_{0.98}\text{S}_2$  (2% V doping) and  $\text{V}_{0.04}\text{Mo}_{0.96}\text{S}_2$  (4% V doping) monolayers. Various combinations for the combined effect of point defects and dopants within the  $\text{MoS}_2$  layer are also taken by constructing  $\text{V}_{0.02}\text{Mo}_{0.98}\text{S}_2 + \text{V}_\text{S}$  (2% V doping and a S monovacancy),  $\text{V}_{0.02}\text{Mo}_{0.98}\text{S}_2 + \text{V}_{\text{S-S}}$  (2% V doping and two adjacent S vacancies on the same layer),  $\text{V}_{0.02}\text{Mo}_{0.98}\text{S}_2 + \text{V}_{2\text{S}}$  (2% V doping and two adjacent S vacancies on the different layer),  $\text{V}_{0.02}\text{Mo}_{0.98}\text{S}_2 + \text{V}_\text{Mo}$  (2% V doping and a Mo monovacancy), and  $\text{V}_{0.02}\text{Mo}_{0.98}\text{S}_2 + \text{V}_{\text{Mo+2S}}$  (with 2% V doping, a Mo vacancy and two adjacent S vacancies on the different layers) monolayers.

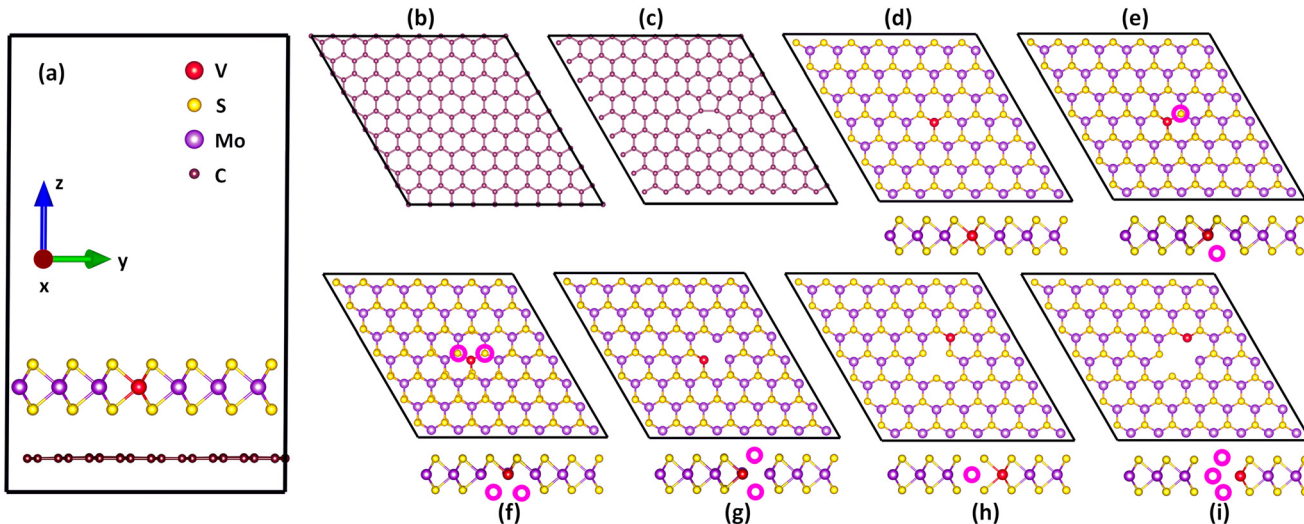
In this study, we simulate HSTs composed of various combinations of Gr and TMDC sheets discussed above. We find that the magnetic properties of HSTs composed of different TMDCs and pristine Gr or Gr +  $\text{V}_{2\text{C}}$  or Gr +  $\text{V}_{\text{SW}}$  are very similar due to the similar nonmagnetic nature of these Gr sheets. Thus, in what follows, we only consider HSTs composed of different TMDCs and pristine Gr or Gr +  $\text{V}_\text{C}$ . The full list of the simulated HSTs composed of various combinations of defective and/or doped monolayers is given in Table 1, and several representative examples of the lattice configurations are shown in Fig. 1. The numerous combinations (26 structures altogether) help us to understand the complex interplay between the types of point defects in a specific monolayer and the magnetic dopants in the Gr/ $\text{MoS}_2$  HSTs.

Table 1 shows the lattice mismatch of each HST by giving the strain each layer experiences in the supercell after full relaxation. It appears that upon the formation of the different HSTs, the Gr layer is shrunk while the TMDC layer is

**Table 1** Built-in strain in each monolayer calculated using  $\varepsilon = \frac{a_{\text{HST}} - a_i}{a_i} \times 100\%$  ( $a_{\text{HST}}$  – lattice constant of the HST;  $a_i$  – lattice constant of the Gr or TMDC layers)

Name	Gr strain (%)	TMDC strain (%)	Name	Gr + $\text{V}_\text{C}$ strain (%)	TMDC strain (%)
HST1: Gr/ $\text{MoS}_2$	-0.234	0.498	HST14: (Gr + $\text{V}_\text{C}$ )/ $\text{MoS}_2$	-0.225	0.530
HST2: Gr/( $\text{MoS}_2 + \text{V}_\text{S}$ )	-0.283	0.644	HST15: (Gr + $\text{V}_\text{C}$ )/( $\text{MoS}_2 + \text{V}_\text{S}$ )	-0.288	0.654
HST3: Gr/( $\text{MoS}_2 + \text{V}_{\text{S-S}}$ )	-0.337	0.824	HST16: (Gr + $\text{V}_\text{C}$ )/( $\text{MoS}_2 + \text{V}_{\text{S-S}}$ )	-0.351	0.833
HST4: Gr/( $\text{MoS}_2 + \text{V}_{2\text{S}}$ )	-0.342	0.778	HST17: (Gr + $\text{V}_\text{C}$ )/( $\text{MoS}_2 + \text{V}_{2\text{S}}$ )	-0.342	0.782
HST5: Gr/( $\text{MoS}_2 + \text{V}_\text{Mo}$ )	-0.220	0.489	HST18: (Gr + $\text{V}_\text{C}$ )/( $\text{MoS}_2 + \text{V}_\text{Mo}$ )	-0.197	0.534
HST6: Gr/( $\text{MoS}_2 + \text{V}_{\text{Mo+2S}}$ )	-0.382	0.806	HST19: (Gr + $\text{V}_\text{C}$ )/( $\text{MoS}_2 + \text{V}_{\text{Mo+2S}}$ )	-0.697	0.708
HST7: Gr/ $\text{V}_{0.02}\text{Mo}_{0.98}\text{S}_2$	-0.247	0.426	HST20: (Gr + $\text{V}_\text{C}$ )/ $\text{V}_{0.02}\text{Mo}_{0.98}\text{S}_2$	-0.234	0.462
HST8: Gr/ $\text{V}_{0.04}\text{Mo}_{0.96}\text{S}_2$	-0.229	0.389	HST21: (Gr + $\text{V}_\text{C}$ )/ $\text{V}_{0.0}\text{Mo}_{0.96}\text{S}_2$	-0.499	0.407
HST9: Gr/( $\text{V}_{0.02}\text{Mo}_{0.98}\text{S}_2 + \text{V}_\text{S}$ )	-0.288	0.535	HST22: (Gr + $\text{V}_\text{C}$ )/( $\text{V}_{0.02}\text{Mo}_{0.98}\text{S}_2 + \text{V}_\text{S}$ )	-0.306	0.512
HST10: Gr/( $\text{V}_{0.02}\text{Mo}_{0.98}\text{S}_2 + \text{V}_{\text{S-S}}$ )	-0.351	0.723	HST23: (Gr + $\text{V}_\text{C}$ )/( $\text{V}_{0.02}\text{Mo}_{0.98}\text{S}_2 + \text{V}_{\text{S-S}}$ )	-0.373	0.723
HST11: Gr/( $\text{V}_{0.02}\text{Mo}_{0.98}\text{S}_2 + \text{V}_{2\text{S}}$ )	-0.346	0.714	HST24: (Gr + $\text{V}_\text{C}$ )/( $\text{V}_{0.02}\text{Mo}_{0.98}\text{S}_2 + \text{V}_{2\text{S}}$ )	-0.364	0.695
HST12: Gr/( $\text{V}_{0.02}\text{Mo}_{0.98}\text{S}_2 + \text{V}_\text{Mo}$ )	-0.234	0.631	HST25: (Gr + $\text{V}_\text{C}$ )/( $\text{V}_{0.02}\text{Mo}_{0.98}\text{S}_2 + \text{V}_\text{Mo}$ )	-0.184	0.480
HST13: Gr/( $\text{V}_{0.02}\text{Mo}_{0.98}\text{S}_2 + \text{V}_{\text{Mo+2S}}$ )	-0.292	0.800	HST26: (Gr + $\text{V}_\text{C}$ )/( $\text{V}_{0.02}\text{Mo}_{0.98}\text{S}_2 + \text{V}_{\text{Mo+2S}}$ )	-0.306	0.809





**Fig. 1** (a) Side view of the pristine HST showing labels for the different atoms and the interlayer separation  $d$ . Top views of the Gr monolayers as part of the V-doped  $\text{MoS}_2/\text{gr}$  HSTs: (b) pristine Gr, (c)  $\text{Gr} + \text{V}_\text{C}$  (with C monovacancy). Top and side views of the various  $\text{V}_{0.02}\text{Mo}_{0.98}\text{S}_2$  monolayers as part of the V-doped  $\text{MoS}_2/\text{Gr}$  HSTs: (d)  $\text{V}_{0.02}\text{Mo}_{0.98}\text{S}_2$  (with 2% V substitutional doping), (e)  $\text{V}_{0.02}\text{Mo}_{0.98}\text{S}_2 + \text{V}_\text{S}$  (with 2% V substitutional doping and S monovacancy), (f)  $\text{V}_{0.02}\text{Mo}_{0.98}\text{S}_2 + \text{V}_\text{S-S}$  (with 2% V doping and S divacancies on the same atomic layer), (g)  $\text{V}_{0.02}\text{Mo}_{0.98}\text{S}_2 + \text{V}_{2\text{S}}$  (with 2% V substitutional doping and S divacancies on different atomic layers), (h)  $\text{V}_{0.02}\text{Mo}_{0.98}\text{S}_2 + \text{V}_\text{Mo}$  (with 2% substitutional V doping and Mo monovacancy), (i)  $\text{V}_{0.02}\text{Mo}_{0.98}\text{S}_2 + \text{V}_{\text{Mo}+2\text{S}}$  (with 2% V doping and an Mo + 2S defect complex). The larger pink circles represent S vacancies.

expanded, but in all cases the effect is less than a percent. For example,  $\text{V}_{0.02}\text{Mo}_{0.98}\text{S}_2$  sheet in  $\text{Gr}/\text{V}_{0.02}\text{Mo}_{0.98}\text{S}_2$  HST is stretched by 0.426%, whereas the Gr sheet is compressed by 0.247% from the optimized pristine cell parameters.  $\text{V}_{0.02}\text{Mo}_{0.98}\text{S}_2$  sheet in  $(\text{Gr} + \text{V}_\text{C})/\text{V}_{0.02}\text{Mo}_{0.98}\text{S}_2$  HST is stretched by 0.462%, while the Gr sheet is compressed by 0.234% from the optimized parameters of the pristine cell. These rather small values for the built-in stress (less than 1% overall) do not change the properties of the monolayers and their HSTs, in agreement with other similar systems.<sup>23</sup>

To gain some insight into the interface properties of the HSTs, we compute the interlayer binding energy using the relation  $E_\text{b} = (E_\text{HST} - E_{\text{L}1} - E_{\text{L}2})/N$ , where  $E_\text{HST}$  is the total energy of each HST,  $E_{\text{L}1,2}$  are the total energies for the individual monolayers, and  $N$  is the number of atoms in the system. Fig. 2 displays  $E_\text{b}$  versus the interlayer separation  $d$  for all systems. The results show that the binding energy is in the range  $E_\text{b} = (-30.152, -26.772)$  meV per atom, while the interlayer separation varies in  $d = (2.885, 3.334)$  Å range. The stability of all HSTs is reflected in the negative values of  $E_\text{b}$ , and we find that those systems containing  $\text{MoS}_2$  with a S monovacancy or divacancies have the highest binding energy. On the other hand, the lowest binding energy is found for systems containing  $\text{MoS}_2$  with a Mo + 2S vacancy complex or V dopants, indicating that such HSTs have a better structural stability compared to the rest of the systems. These  $E_\text{b}$  values are typical for HSTs in which van der Waals (vdW) interactions play an important role in their structural stability.<sup>24</sup>

The interlayer separation in all cases is also in the typical vdW range, since for all systems  $d$  is found to be greater than the sum of the covalent radii of C and S atoms (0.76 and 1.05 Å, respectively). For  $\text{Gr}/\text{V}_{0.04}\text{Mo}_{0.96}\text{S}_2$  HST,  $d$  is very similar to

the case of the pristine  $\text{Gr}/\text{V}_{0.02}\text{Mo}_{0.98}\text{S}_2$  HST. However, it appears that  $d$  between Gr and defective  $\text{V}_{0.02}\text{Mo}_{0.98}\text{S}_2$  monolayers is smaller as compared to the one for the pristine  $\text{Gr}/\text{V}_{0.02}\text{Mo}_{0.98}\text{S}_2$  HST. This effect becomes more pronounced for the defective Gr.

## 2.2 Magnetic properties

The interplay between defects and dopants also affects the magnetic properties of the studied HSTs. Our calculations show that several materials exhibit a ferromagnetic ordering, and in Fig. 3 we show results for the total magnetic moment of the system  $M_\text{tot}$ , and the total magnetic moment for the corresponding Gr layer,  $M_\text{Gr}$ , and TMDC layer,  $M_\text{TMDC}$ .

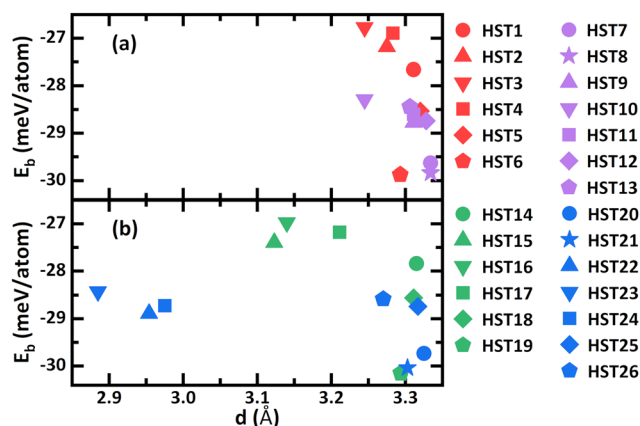


**Fig. 2** Interlayer binding energy  $E_\text{b}$  (eV) as a function of the interlayer separation  $d$  (Å) of HSTs: (a) Gr/TMDCs and (b)  $(\text{Gr} + \text{V}_\text{C})/\text{TMDCs}$ .



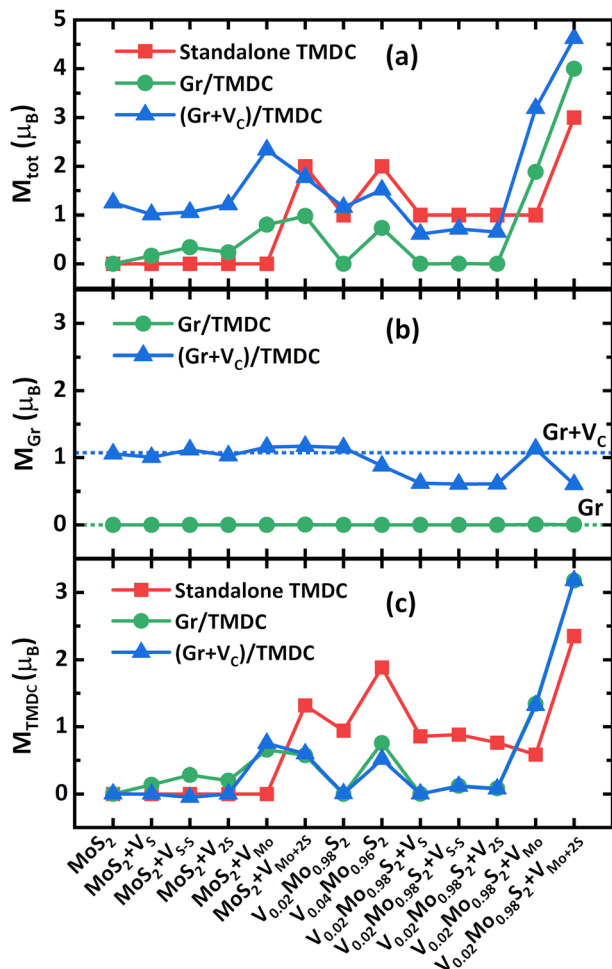


Fig. 3 Magnetic moments of the: (a) entire HST  $M_{\text{tot}}$  ( $\mu_{\text{B}}$ ), (b) Gr layer  $M_{\text{Gr}}$  ( $\mu_{\text{B}}$ ), (c) TMDC layer  $M_{\text{TMDC}}$  ( $\mu_{\text{B}}$ ) as part of HSTs. The data is given as a function of the different TMDC used to construct each HST.

Let us first examine the isolated  $\text{MoS}_2$  monolayer. From the calculations, we find that isolated S monovacancy and divacancies, and Mo monovacancy do not induce magnetic ordering in the isolated TMDC monolayer. This agrees with previous studies on defective and single-doped  $\text{MoS}_2$ .<sup>25</sup> The total magnetic moment is  $2 \mu_{\text{B}}$  for  $\text{MoS}_2 + \text{V}_{\text{Mo}+2\text{S}}$ . On the other hand,  $M_{\text{tot}} = 1 \mu_{\text{B}}$  for a V-doped  $\text{MoS}_2$  with or without S monovacancy, S divacancies, Mo monovacancy ( $\text{V}_{0.02}\text{Mo}_{0.98}\text{S}_2$ ,  $\text{V}_{0.02}\text{Mo}_{0.98}\text{S}_2 + \text{V}_s$ ,  $\text{V}_{0.02}\text{Mo}_{0.98}\text{S}_2 + \text{V}_{\text{S-S}}$ ,  $\text{V}_{0.02}\text{Mo}_{0.98}\text{S}_2 + \text{V}_{2\text{S}}$ ,  $\text{V}_{0.02}\text{Mo}_{0.98}\text{S}_2 + \text{V}_{\text{Mo}}$ ). Increasing of the doping concentration raises  $M_{\text{tot}}$  to  $2 \mu_{\text{B}}$  for  $\text{V}_{0.04}\text{Mo}_{0.96}\text{S}_2$ , while  $M_{\text{tot}} = 3 \mu_{\text{B}}$  for  $\text{V}_{0.02}\text{Mo}_{0.98}\text{S}_2 + \text{V}_{\text{Mo}+2\text{S}}$ . Such synergistic effects have been observed experimentally.<sup>26</sup>

This situation changes upon the HST formation by adding a Gr layer. In fact, Fig. 3 shows that there is a tendency of reducing the total magnetization when a pristine Gr is stacked above a  $\text{MoS}_2$  with mono or divacancies despite their V dopants. It is interesting to observe that  $M_{\text{tot}} = 1 \mu_{\text{B}}$  of the stand-alone  $\text{V}_{0.02}\text{Mo}_{0.98}\text{S}_2$  becomes  $M_{\text{tot}} = 0$  for  $\text{Gr}/\text{V}_{0.02}\text{Mo}_{0.98}\text{S}_2$ . In other words, a ferromagnetic standalone  $\text{MoS}_2$  with a 2% V doping becomes nonmagnetic upon bringing Gr together (HST7). Fig. 3

also shows that this trend holds for  $\text{Gr}/(\text{V}_{0.02}\text{Mo}_{0.98}\text{S}_2 + \text{V}_s)$ ,  $\text{Gr}/(\text{V}_{0.02}\text{Mo}_{0.98}\text{S}_2 + \text{V}_{\text{S-S}})$ ,  $\text{Gr}/(\text{V}_{0.02}\text{Mo}_{0.98}\text{S}_2 + \text{V}_{2\text{S}})$  (HST9, 10, 11), thus S mono and divacancies in the 2% doped TMDC do not affect the overall lack of magnetic moment in the HSTs. Moreover,  $M_{\text{tot}} = 2 \mu_{\text{B}}$  of the stand-alone  $\text{V}_{0.04}\text{Mo}_{0.96}\text{S}_2$  becomes  $M_{\text{tot}} = 0.736 \mu_{\text{B}}$  for  $\text{Gr}/\text{V}_{0.04}\text{Mo}_{0.96}\text{S}_2$ . This reduction in the total magnetic moment is directly associated with charge transfer from Gr to V-doped  $\text{MoS}_2$  layer regardless of point defect presence, as discussed below. Nevertheless, there are situations where the Gr layer enhances the FM properties of the standalone TMDC. Such is the case of a V-doped  $\text{MoS}_2$  with a Mo monovacancy or a Mo + 2S complex defect. The Gr monolayer enhances the  $M_{\text{tot}}$  by about 88% and 33% when compared to the isolated  $\text{V}_{0.02}\text{Mo}_{0.98}\text{S}_2 + \text{V}_{\text{Mo}}$  or  $\text{V}_{0.02}\text{Mo}_{0.98}\text{S}_2 + \text{V}_{\text{Mo}+2\text{S}}$ . Fig. 3b and c show that in all HSTs containing a pristine Gr monolayer, the magnetic properties are carried out by the TMDC monolayer, and Gr remains nonmagnetic.

The magnetic properties of the HSTs with a defective Gr layer are overall greatly enhanced compared with those of the standalone TMDC layer and the HST with the pristine Gr layer. We find that the total magnetic moment of Gr with C monovacancy is  $1.271 \mu_{\text{B}}$ . The FM state of  $(\text{Gr} + \text{V}_c)$  agrees with the well-known Lieb theorem that C monovacancy induces a magnetic moment on Gr while other defects do not.<sup>27,28</sup> We further find that  $(\text{Gr} + \text{V}_c)/\text{TMDC}$  with the S point defects shows a prominent ferromagnetism with  $M_{\text{tot}} > 1 \mu_{\text{B}}$  unlike the nonmagnetic TMDC monolayer or the weakly ferromagnetic Gr/TMDC system. This enhancement effect is even stronger for the  $(\text{Gr} + \text{V}_c)/(\text{MoS}_2 + \text{V}_{\text{Mo}})$  and  $(\text{Gr} + \text{V}_c)/(\text{MoS}_2 + \text{V}_{\text{Mo}+2\text{S}})$ . The magnetic moments for  $(\text{Gr} + \text{V}_c)/\text{V}_{0.02}\text{Mo}_{0.98}\text{S}_2$  and  $(\text{Gr} + \text{V}_c)/\text{V}_{0.04}\text{Mo}_{0.96}\text{S}_2$  are  $1.157$  and  $1.513 \mu_{\text{B}}$ , respectively. It is also interesting to note that the defective Gr has elevated  $M_{\text{tot}}$  for its HSTs formed with a doped TMDC with  $(\text{Gr} + \text{V}_c)/(\text{V}_{0.02}\text{Mo}_{0.98}\text{S}_2 + \text{V}_{\text{Mo}})$  and  $(\text{Gr} + \text{V}_c)/(\text{V}_{0.02}\text{Mo}_{0.98}\text{S}_2 + \text{V}_{\text{Mo}+2\text{S}})$  defects, for which Gr/TMDC showed weak ferromagnetism. It appears that in such cases, the magnetization is carried out primarily by the defective Gr layer (Fig. 3b and c). Introducing V dopants, however, enhances the magnetization of the TMDC layer itself, while  $\text{Gr} + \text{V}_c$  remains ferromagnetic as well. Thus, these results show that the C vacancy plays a key role in the overall magnetic properties of the entire HST because it enhances the magnetization of the Gr layer itself. Such enhancement due to the ferromagnetism of the defective Gr layer is consistent with the enhanced magnetism found in other HSTs involving TMDC monolayers and ferromagnetic layers.<sup>15,29,30</sup>

Further insight of the ferromagnetism of these systems can be gained by examining the electron spin density property. In Fig. 4, we show some representative cases by giving the electron spin density distribution with TMDC on top of the Gr layer.  $\text{Gr}/\text{V}_{0.02}\text{Mo}_{0.98}\text{S}_2$  is non-magnetic and no spin density appears between atoms in this system (Fig. 4a). The nearest Mo-site spins are antiferromagnetically coupled to the V-site spin, while the nearest S-site spins are ferromagnetically coupled to the V-site spin in  $\text{V}_{0.04}\text{Mo}_{0.96}\text{S}_2$  monolayer. However, both the nearest Mo and S-site spins couple antiferromagnetically with the V-site spin in  $\text{V}_{0.02}\text{Mo}_{0.98}\text{S}_2$  layer of  $\text{Gr}/\text{V}_{0.04}\text{Mo}_{0.96}\text{S}_2$  HST



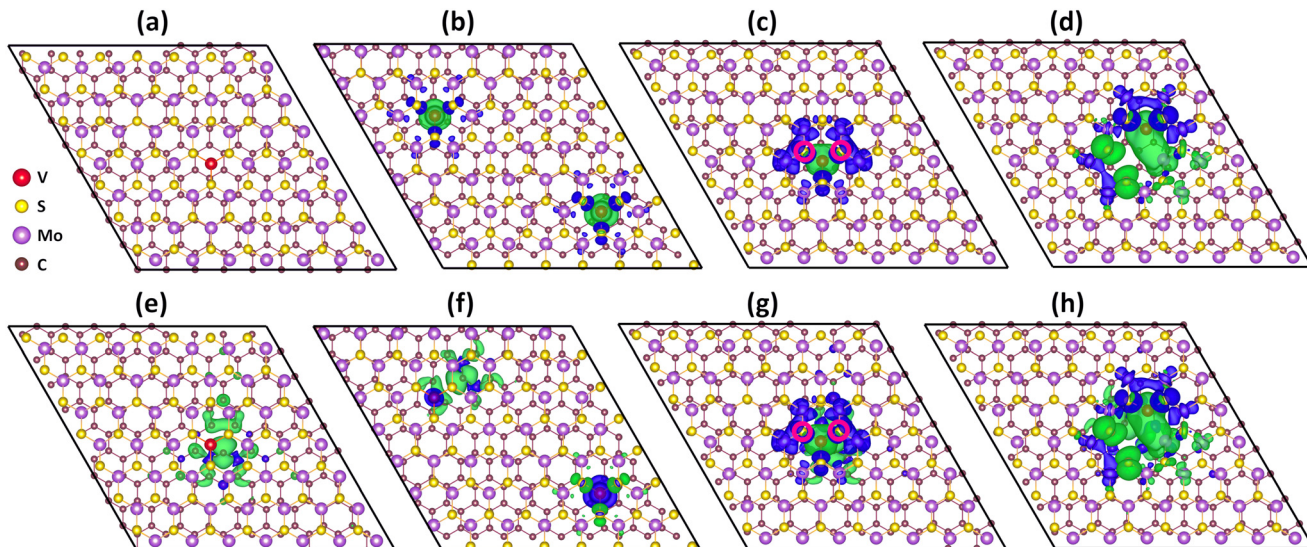


**Fig. 4** Electron spin densities of: (a)  $\text{Gr}/\text{V}_{0.02}\text{Mo}_{0.98}\text{S}_2$ , (b)  $\text{Gr}/\text{V}_{0.04}\text{Mo}_{0.96}\text{S}_2$ , (c)  $\text{Gr}/(\text{V}_{0.02}\text{Mo}_{0.98}\text{S}_2 + \text{V}_{\text{S-S}})$ , (d)  $\text{Gr}/(\text{V}_{0.02}\text{Mo}_{0.98}\text{S}_2 + \text{V}_{\text{Mo+2S}})$ , (e)  $(\text{Gr} + \text{V}_\text{C})/\text{V}_{0.02}\text{Mo}_{0.98}\text{S}_2$ , (f)  $(\text{Gr} + \text{V}_\text{C})/\text{V}_{0.04}\text{Mo}_{0.96}\text{S}_2$ , (g)  $(\text{Gr} + \text{V}_\text{C})/(\text{V}_{0.02}\text{Mo}_{0.98}\text{S}_2 + \text{V}_{\text{S-S}})$  and (h)  $(\text{Gr} + \text{V}_\text{C})/(\text{V}_{0.02}\text{Mo}_{0.98}\text{S}_2 + \text{V}_{\text{Mo+2S}})$  HSTs. Green and blue colors represent the spin-up and spin-down charges, respectively. The pink circles represent S vacancy positions. The isosurface value is  $10^{-3} \text{ e } \text{\AA}^{-3}$ .

(Fig. 4b). Although the  $\text{Gr}/(\text{V}_{0.02}\text{Mo}_{0.98}\text{S}_2 + \text{V}_{\text{S-S}})$  HST has a total magnetic moment of zero, the antiferromagnetic orders appeared around the V atom ( $0.807 \mu_\text{B}$ ) in the TMDC layer (Fig. 4c). In  $\text{V}_{0.02}\text{Mo}_{0.98}\text{S}_2 + \text{V}_{\text{Mo+2S}}$  sheet of  $\text{Gr}/(\text{V}_{0.02}\text{Mo}_{0.98}\text{S}_2 + \text{V}_{\text{Mo+2S}})$  HST, the antiferromagnetic orders appeared on the nearest Mo and S atoms around V atom, while the ferromagnetic orders appeared on the nearest Mo and S atoms around vacancy. In this case, we can clearly see that the spin density is located not only on the atoms but also on the empty spaces (Fig. 4d). Spin density distributions are not found in the Gr sheets of these HSTs, which are consistent with the values shown in Fig. 3b. For defective Gr sheet of  $(\text{Gr} + \text{V}_\text{C})/\text{TMDC}$  HSTs, the C monovacancy produces two pentagons while the FM order is observed in one pentagon and the AFM order is observed in another pentagon (Fig. 4e-h). In  $(\text{Gr} + \text{V}_\text{C})/\text{V}_{0.02}\text{Mo}_{0.98}\text{S}_2$  HST, no spin density is observed in  $\text{V}_{0.02}\text{Mo}_{0.98}\text{S}_2$  component (Fig. 4e). In  $(\text{Gr} + \text{V}_\text{C})/\text{V}_{0.04}\text{Mo}_{0.96}\text{S}_2$  HST, both V atoms have negative magnetic moments, but only one AFM order is observed for the nearest Mo and S atoms (Fig. 4f). Interestingly, spin density distributions of  $\text{V}_{0.02}\text{Mo}_{0.98}\text{S}_2 + \text{V}_{\text{S-S}}$  or  $\text{V}_{0.02}\text{Mo}_{0.98}\text{S}_2 + \text{V}_{\text{Mo+2S}}$  are almost unchanged in HSTs with the pristine or defective Gr sheets (Fig. 4g and h).

We also examined the magnetic moments of  $\text{V}_{0.02}\text{Mo}_{0.98}\text{S}_2$  with various vacancies placed on Gr with C divacancies or SW defect and found that the magnetic phenomena in these systems are similar to those observed in pristine Gr. This is because the three systems pristine Gr,  $\text{Gr} + \text{V}_{2\text{C}}$  and  $\text{Gr} + \text{V}_{\text{SW}}$  are nonmagnetic.

### 2.3 Electronic structures properties

We further discuss the electronic properties of the HSTs by analyzing their band structures (Fig. 5 and 6). For better clarity, the band structures for the individual layers in each

HST are presented. Metallic behavior is observed for all cases except for the pristine Gr/MoS<sub>2</sub> showing to be a semi-metal (Fig. 5a). In all cases, the well-known Dirac cones of an isolated Gr monolayer are maintained upon HST formation with the TMDC.

Fig. 5b shows that V doping is responsible for the electronic state of  $\text{Gr}/\text{V}_{0.02}\text{Mo}_{0.98}\text{S}_2$  HST becoming metallic. There is an upward shift of the electron states occupied in the valence band of the TMDC layer compared to that of the pristine HST, confirming the electron depletion from the Gr to the  $\text{V}_{0.02}\text{Mo}_{0.98}\text{S}_2$  sheet. Increasing the concentration of V doping causes the electron states occupied in the valence band to continue to shift upward, resulting in an impurity state near the Fermi level (Fig. 5c). For  $\text{Gr}/\text{V}_{0.02}\text{Mo}_{0.98}\text{S}_2$  with vacancies, the defective states appear mainly in the gap region of the  $\text{V}_{0.02}\text{Mo}_{0.98}\text{S}_2$  system (Fig. 5d).

The band structures of the defective Gr in  $(\text{Gr} + \text{V}_\text{C})/\text{TMDC}$  HSTs show that the bands for both spin carriers cross the Fermi energy (near the  $\Gamma$  point) (Fig. 6). Similarly to Gr, the band structures of  $\text{Gr} + \text{V}_\text{C}$  in these HSTs show upward shifts of the Dirac points. The position of the Dirac points above the Fermi level reflects the number of electrons transferred from the  $\text{Gr} + \text{V}_\text{C}$  to the TMDC monolayer. A notable difference between the band structures of  $\text{Gr} + \text{V}_\text{C}$  in these HSTs is the different locations of the  $\sigma$  bands around the energy range of  $-1$  to  $-0.5$  eV. The band structures of the TMDC components in  $(\text{Gr} + \text{V}_\text{C})/\text{TMDC}$  HSTs are almost unchanged compared to those in Gr/TMDC HSTs.

Upon the introduction of the C monovacancy in Gr as part of each HST, one of linear  $\pi-\pi^*$  crossing bands breaks its degeneracy turning it into a quadratically dispersing one (Fig. 6). The spin-splitting gap between these bands depends on the V doping and vacancy concentrations in the TMDC layer. In particular, the introduction of V dopants at 2%



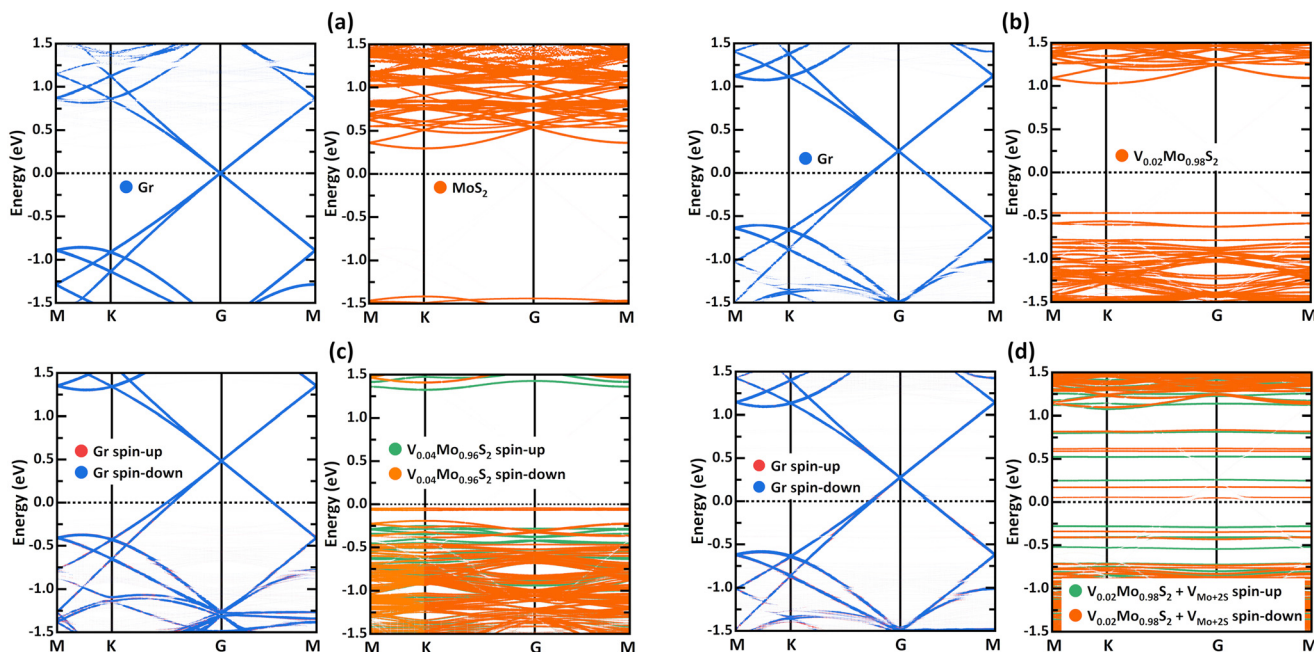


Fig. 5 Band structures of (a)  $Gr/MoS_2$ , (b)  $Gr/V_{0.02}Mo_{0.98}S_2$ , (c)  $Gr/V_{0.04}Mo_{0.96}S_2$  and (d)  $Gr/(V_{0.02}Mo_{0.98}S_2 + V_{Mo+2S})$  HSTs where the dotted lines represent the Fermi level.

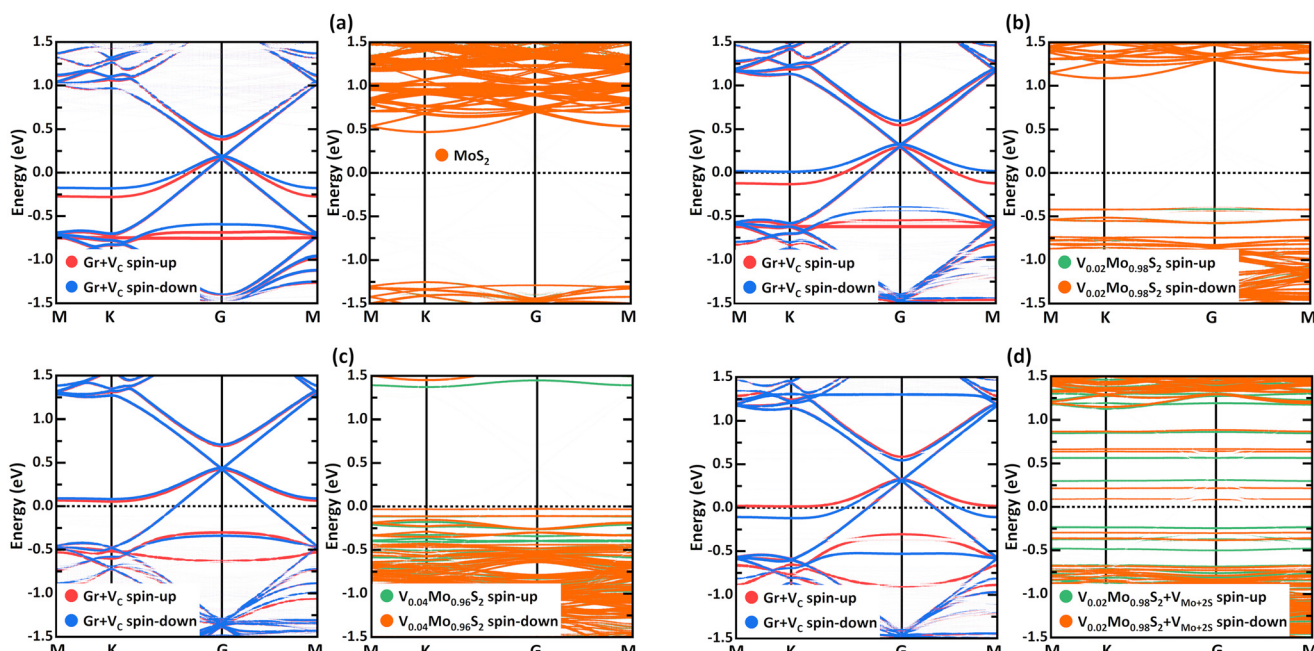


Fig. 6 Band structures of (a)  $(Gr + V_c)/MoS_2$ , (b)  $(Gr + V_c)/V_{0.02}Mo_{0.98}S_2$ , (c)  $(Gr + V_c)/V_{0.04}Mo_{0.96}S_2$  and (d)  $(Gr + V_c)/(V_{0.02}Mo_{0.98}S_2 + V_{Mo+2S})$  HSTs where the dotted lines represent the Fermi level.

concentration (Fig. 6b) increases the spin splitting gap while 4% concentration of V dopants (Fig. 6c) reduces the spin splitting gap when compared to the pristine TMDC (Fig. 6a). In the  $(Gr + V_c)/V_{0.02}Mo_{0.98}S_2$  HST (Fig. 6b), the Fermi level crosses the spin-up  $\pi$  band but lies completely below the entire spin-down  $\pi$  band, which causes a slight increase in the defective Gr magnetism. On the other hand, in the  $(Gr +$

$V_c)/V_{0.04}Mo_{0.96}S_2$  HST (Fig. 6c), the Fermi level lies completely below both spin-up and -down  $\pi$  bands and leads to a small reduction in the defective Gr magnetism. Furthermore, when  $(Mo + 2S)$  vacancies are present in the V dopants with 2% concentration (Fig. 6d), the splitting of  $\pi$  and  $\pi^*$  bands is similar to that in defect-free HST (Fig. 6b). However, the  $(Mo + 2S)$  vacancies in TMDC layer reverses the spin polarizations

of the  $\pi$  and  $\pi^*$  bands. This reversal reduces the magnetism in the defective Gr layer in  $(\text{Gr} + \text{V}_\text{C})/(\text{V}_{0.02}\text{Mo}_{0.98}\text{S}_2 + \text{V}_{\text{Mo}+2\text{S}})$  HST compared to the corresponding defect-free  $(\text{Gr} + \text{V}_\text{C})/\text{V}_{0.02}\text{Mo}_{0.98}\text{S}_2$  HST.

The charge transfer in each HST is closely related to its electronic structure; thus, we also calculate the 3D charge density differences in each case. The results are shown in Fig. 7. We find that generally electrons are transferred from Gr or  $(\text{Gr} + \text{V}_\text{C})$  to the TMDC monolayer. No significant charge transfer is observed between Gr and  $\text{MoS}_2$  (Fig. 7a), which is also found experimentally.<sup>31</sup> Significant charge transfer is observed between the Gr and  $\text{V}_{0.02}\text{Mo}_{0.98}\text{S}_2$  (Fig. 7b). The creation of vacancies or the increase in the doping concentration of V also significantly increases the charge transfer between the Gr and the TMDC layers (Fig. 7c and d). This is consistent with previous theoretical and experimental papers in other HSTs involving V-doped TMDCs ( $\text{Fe}/\text{W}_{0.967}\text{V}_{0.033}\text{Se}_2/\text{Pt}$ ,  $\text{Bi}_2\text{O}_2\text{Se}/\text{WS}_2\text{-V}$ ).<sup>29,32</sup> The charge transfers between the defective Gr and TMDCs are comparatively higher than those observed between the pristine Gr and TMDCs (Fig. 7e–h). We can see that a significant portion of the charge density is localized on the C atoms near the defect sites, which results in a stronger interaction between the defective Gr and TMDC HSTs.

#### 2.4 Experimental observation of enhanced magnetization in V-doped $\text{MoS}_2$ /graphene heterostructures

To experimentally validate the DFT calculations of increased magnetization in the defective and doped  $\text{MoS}_2/\text{Gr}$  HSTs, we also report measurements of the V-doped  $\text{MoS}_2$  monolayers and V-doped  $\text{MoS}_2/\text{Gr}$  HSTs alongside reference samples including pristine  $\text{MoS}_2$  monolayers and  $\text{MoS}_2/\text{Gr}$  system. Details on the growth processes of these samples are provided in the Experimental Methods section. Magnetic measurements were carried out using a vibrating sample magnetometry (VSM) probe integrated into a physical property measurement system (PPMS) over a temperature range of 10–300 K. In all magnetic measurements, the magnetic field was applied parallel to the plane of the monolayer films. The results are given in Fig. 8(a–d).

We observed that shown 2% vanadium doping induces FM ordering at room temperature, resulting in enhanced saturation magnetization  $M_\text{S}$  in the V-doped  $\text{MoS}_2$  (Fig. 8a) compared to the pristine  $\text{MoS}_2$  monolayer (Fig. 8d). As expected, pristine  $\text{MoS}_2$  monolayers grown on  $\text{Si}/\text{SiO}_2$  substrates exhibit a weak FM signal, likely originating from various intrinsic vacancy defects.<sup>14,33</sup> Our DFT calculations support this, showing that specific defect configurations (e.g.  $\text{V}_{\text{Mo}+2\text{S}}$  vacancies) dominantly induce FM ordering in the  $\text{MoS}_2$  monolayer. Other studies have also shown that the  $\text{MoS}_2$  net magnetic moment increases proportionally with the density of  $\text{V}_{\text{Mo}+2\text{S}}$  vacancies.<sup>34</sup> Experiments have indeed demonstrated the presence of S and/or Mo vacancies in CVD-grown  $\text{MoS}_2$  and V-doped  $\text{MoS}_2$  monolayers.<sup>14,26</sup>

Notably, when the V-doped  $\text{MoS}_2$  monolayer is stacked with graphene, the  $M_\text{S}$  increases dramatically in the HST compared to the V-doped monolayer alone (Fig. 8a and b). At room temperature  $M_\text{S}$  increases from  $\sim 5.67 \mu\text{emu cm}^{-2}$  in the doped TMDC to  $\sim 55.83 \mu\text{emu cm}^{-2}$  in the HST. As shown in Fig. 8c, this enhancement persists across the full temperature range of 10–300 K. Moreover, the  $M_\text{S}$  of the V-doped  $\text{MoS}_2/\text{Gr}$  system (Fig. 8a) is nearly doubled of the undoped  $\text{MoS}_2/\text{Gr}$  (Fig. 8d). Compared to the isolated  $\text{MoS}_2$  or V-doped  $\text{MoS}_2$  monolayers, the increase in magnetization upon interfacing with graphene in our HSTs is also consistent with reports on TMDC/Gr systems.<sup>15,16</sup> For example, Cai *et al.*<sup>16</sup> suggest that covalent interactions at the  $\text{MoS}_2$  Moiré superlattice/graphene oxide interface, such as the formation of Mo–S–C bonds, lead to spin polarization of Mo 4d electrons near the Fermi level, thereby inducing high-temperature FM ordering in the HST. However, such interfacial effects alone cannot explain the substantial  $M_\text{S}$  enhancement observed in our  $\text{MoS}_2/\text{Gr}$  systems (Fig. 8a and d). The study<sup>15</sup> has demonstrated that vacancy defects play a critical role in inducing ferromagnetic ordering in the  $\text{MoS}_2$  monolayer as part of Mn-doped  $\text{MoS}_2/\text{Gr}$  systems.

A comparison between Fig. 8a and d suggests that the graphene interfacing effect contributes more to the overall magnetization than V-doping alone. The combined effect of V-doping and  $\text{MoS}_2/\text{Gr}$  interfacing results in the highest observed  $M_\text{S}$  in the V-doped  $\text{MoS}_2/\text{Gr}$  HST (see the inset of Fig. 8c),

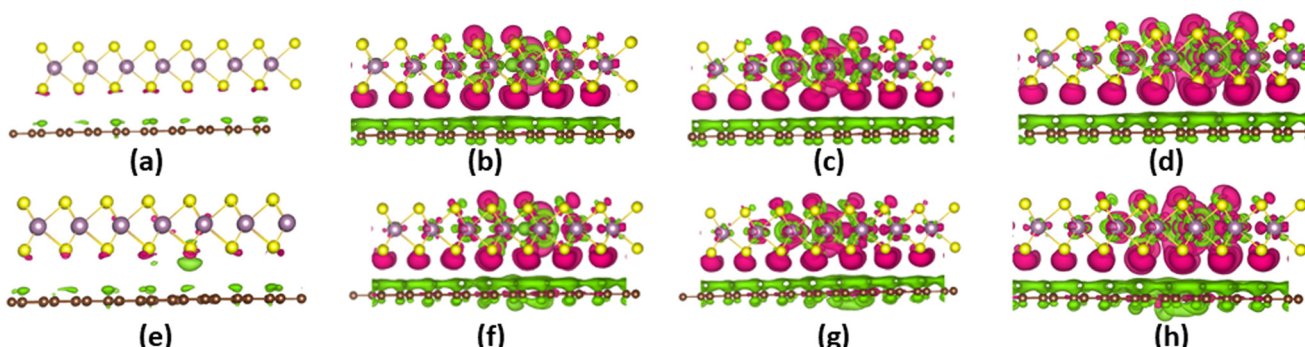
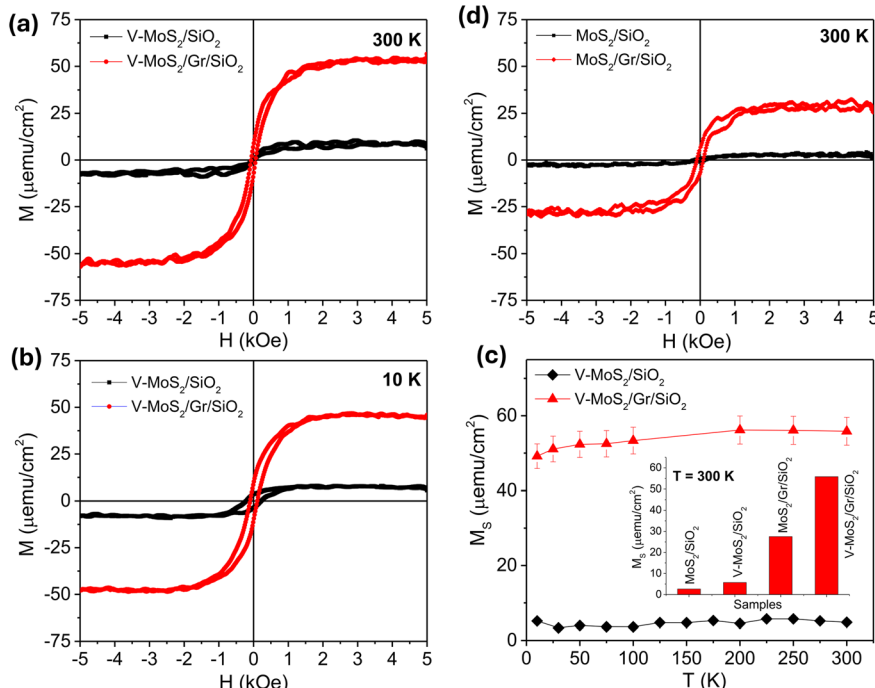


Fig. 7 Charge density differences of (a)  $\text{Gr}/\text{MoS}_2$ , (b)  $\text{Gr}/\text{V}_{0.02}\text{Mo}_{0.98}\text{S}_2$ , (c)  $\text{Gr}/(\text{V}_{0.02}\text{Mo}_{0.98}\text{S}_2 + \text{V}_{\text{Mo}+2\text{S}})$  (d)  $\text{Gr}/\text{V}_{0.04}\text{Mo}_{0.96}\text{S}_2$ , (e)  $(\text{Gr} + \text{V}_\text{C})/\text{MoS}_2$ , (f)  $(\text{Gr} + \text{V}_\text{C})/\text{V}_{0.02}\text{Mo}_{0.98}\text{S}_2$ , (g)  $(\text{Gr} + \text{V}_\text{C})/(\text{V}_{0.02}\text{Mo}_{0.98}\text{S}_2 + \text{V}_{\text{Mo}+2\text{S}})$  and (h)  $(\text{Gr} + \text{V}_\text{C})/\text{V}_{0.04}\text{Mo}_{0.96}\text{S}_2$  HSTs. The isosurface values are  $3 \times 10^{-4} \text{ e } \text{\AA}^{-3}$ . The pink isosurfaces represent the charge accumulation, the green isosurfaces represent the charge depletion.





**Fig. 8** Magnetic hysteresis loops of the V-doped  $\text{MoS}_2$  and V-doped  $\text{MoS}_2/\text{Gr}$  samples at (a) 300 K and (b) 10 K; (c) temperature dependence of saturation magnetization for the V-doped  $\text{MoS}_2$  and V-doped  $\text{MoS}_2/\text{Gr}$  samples; (d) magnetic hysteresis loops taken at 300 K for the  $\text{MoS}_2$  and  $\text{MoS}_2/\text{Gr}$  samples.

surpassing both the V-doped  $\text{MoS}_2$  monolayer and the  $\text{MoS}_2/\text{Gr}$  HST. These experimental observations are fully supported by our DFT simulations, which also predict that the presence of (C, S, Mo) vacancies in both graphene and TMDC layers can enhance the overall magnetization, particularly when these defects are close and located near the interface. Electron transfer from  $\text{MoS}_2$  to graphene further strengthens the FM coupling between V magnetic ions *via* p-d orbital hybridization (Fig. 7b), contributing to the observed magnetization enhancement. Compared to the undoped HST, the charge transfer effect appears significantly stronger in the V-doped  $\text{MoS}_2/\text{Gr}$  system, especially in those with  $\text{V}_{\text{Mo}}$  and  $\text{V}_{\text{Mo}+2\text{S}}$  vacancies. Our combined theoretical and experimental findings not only validate the magnetization enhancement predicted for Mn-doped  $\text{MoS}_2/\text{Gr}$  heterostructures,<sup>15</sup> but also provide new insights into the underlying physical mechanisms driving FM ordering in the 2D TMDC/Gr systems adding new functionalities to 2D van der Waals heterostructure-based nanodevices.<sup>35,36</sup>

### 3 Conclusions

The present study reports on the geometric, electronic and magnetic properties of V-doped  $\text{MoS}_2/\text{Gr}$  HSTs with relatively low V doping. All considered HSTs are metallic in nature, except the pristine  $\text{Gr}/\text{MoS}_2$  showing to be a semi-metal, with charge transfer from the Gr layer to the TMDC layer. This type of charge transfer is enhanced in the defective HSTs with a significant portion of the charge density localized near the defect sites.

We further find that  $\text{Gr}/\text{MoS}_2$  is nonmagnetic when doped with 2% V and becomes ferromagnetic with a total magnetic moment of  $3 \mu_{\text{B}}$  per cell as the V doping concentration increases. The V-doped  $\text{MoS}_2/\text{Gr}$  HST with 4% V doping experiences stronger charge transfer as well as an upshift of the Dirac point. The effects of various defects, such as C monovacancy and Mo, S vacancies on the structural, electronic, and magnetic properties of V-doped  $\text{MoS}_2/\text{Gr}$  HSTs with 2% V doping are also studied. The overall geometry and stability of HSTs change insignificantly in the presence of defects. However, the defects in both Gr and V-doped  $\text{MoS}_2$  control the magnetic properties of the resulting HSTs. Pristine Gr remains nonmagnetic in all studied HSTs, while defective Gr displays strong magnetic properties. On the other hand, S mono and divacancies have secondary effects on the overall magnetization in the Gr/TMDC and (Gr +  $\text{V}_\text{C}$ )/TMDC HSTs, respectively. In contrast, the Mo monovacancy and (Mo + 2S) complex defect in the 2% doped TMDC noticeably affect the overall magnetization in the Gr/TMDC and (Gr +  $\text{V}_\text{C}$ )/TMDC HSTs, respectively.

This study sheds light on the complex magnetism in sharp interfaced HSTs composed of graphene and a TMDC monolayer when doping and defects are taken into account. Tuning ferromagnetism in 2D systems by varying doping concentration and defect engineering is an attractive pathway for targeted applications in spintronics and other areas.

### 4 Methods

#### 4.1 Computational methods

The first-principles calculations are performed in the Vienna *ab initio* simulation package (VASP)<sup>37</sup> based on density functional



theory (DFT)<sup>38</sup> and the projector augmented wave (PAW) method.<sup>39</sup> The PAW potentials describe the core states of C, Mo, S and V by the electronic configurations of [He]2s<sup>2</sup>p<sup>2</sup>, [Ar]4s<sup>2</sup>3-d<sup>10</sup>, [Ne]3s<sup>2</sup>p<sup>4</sup> and [Ar]3d<sup>3</sup>4s<sup>2</sup>, respectively. The Perdew–Burke–Ernzerhof (PBE) parameterization of the generalized gradient approximation (GGA) is employed to describe the exchange–correlation function.<sup>40</sup> The structures have been optimized using the conjugate gradient method with the forces calculated using the Hellman–Feynman theorem. The convergence criteria for the total energy and residual force on each atom are set to 10<sup>-5</sup> eV and 10<sup>-2</sup> eV Å<sup>-1</sup>, respectively. To isolate the interaction between the HST and its periodic images, a vacuum layer with a thickness of 15 Å is inserted along the direction perpendicular to the layers. In addition, the DFT-D3(BJ) approach<sup>41</sup> is used to correct the vdW interaction in the HSTs. Considering the strong correlation effect of the V-3d electrons, a simplified DFT+U approach<sup>42</sup> is employed with  $U_{\text{eff}} = 3$  eV.<sup>29</sup> The plane-wave energy cutoff is set to 500 eV, and a  $\Gamma$ -centered k meshes of 2 × 2 × 1 is adopted to sample the first Brillouin zone for geometry optimization. The total energies and electronic structures are calculated with the optimized structures on a 9 × 9 × 1 Monkhorst–Pack k-grid. The planar-averaged differential charge density offers a quantitative base for analyzing interfacial charge redistribution, which is defined as  $\Delta\rho = \rho_{\text{L1/L2}} - \rho_{\text{L1}} - \rho_{\text{L2}}$  where  $\rho_{\text{L1/L2}}$ ,  $\rho_{\text{L1}}$  and  $\rho_{\text{L2}}$  are the planar-averaged charge density of the HST and the isolated monolayers constituted the HST, respectively.

#### 4.2 Experimental methods

Pristine MoS<sub>2</sub> and V-doped MoS<sub>2</sub> monolayers were synthesized via chemical vapor deposition (CVD) and subsequently wet-transferred onto a CVD-grown graphene monolayer supported on a SiO<sub>2</sub>/Si substrate. A vanadium doping concentration of 2 at% was selected for this study, consistent with our previous work.<sup>14</sup> The vanadium doping level was controlled by adjusting the V:Mo ratio in the precursor mixture. Additional factors such as source placement, temperature gradient, carrier gas flow rate, and substrate positioning were also carefully optimized for the control of the doping concentration. The graphene monolayer was prepared through the thermal decomposition of a carbon-rich precursor, leading to the deposition of carbon atoms in a honeycomb lattice atop a copper film, which served as the catalytic substrate. After growth, the graphene layer was coated with polymethyl methacrylate (PMMA), and the underlying copper was etched away prior to transfer onto the SiO<sub>2</sub>/Si substrate. The MoS<sub>2</sub>/Gr and V-doped MoS<sub>2</sub>/Gr HSTs were annealed at 300 °C for 10 hours to remove PMMA residues introduced during the transfer process. Post-annealing, the interlayer spacing between the V-doped MoS<sub>2</sub> and graphene was measured to be approximately 1.5 nm. For comparison, pristine and V-doped MoS<sub>2</sub> monolayers were also annealed under the same conditions.

The structural properties of both pristine and V-doped TMDC monolayers, as well as their corresponding TMDC/graphene HSTs, were characterized using scanning transmission electron

microscopy (STEM) and atomic force microscopy (AFM). The optical responses were examined via Raman and photoluminescence (PL) spectroscopy. Magnetic properties were measured using a vibrating sample magnetometry (VSM) probe integrated into a physical property measurement system (PPMS), under magnetic fields up to 9 T and across a broad temperature range from 2 K to 400 K.

#### Conflicts of interest

There are no conflicts to declare.

#### Data availability

All data that support the findings of this study have been included in this publication.

#### Acknowledgements

D. T.-X. D. acknowledges financial support from Presidential Fellowship sponsored by University of South Florida. L. M. W. acknowledges financial support from the US Department of Energy under Grant No. DE-FG02-06ER46297. Computational resources are provided by USF Research Computing. M. H. P. acknowledges support from the US Department of Energy, Office of Basic Energy Sciences, Division of Materials Science and Engineering under Grant No. DE-FG02-07ER46438 (magnetic measurements).

#### References

- Y. K. Luo, J. Xu, T. Zhu, G. Wu, E. J. McCormick, W. Zhan, M. R. Neupane and R. K. Kawakami, Opto-valleytronic spin injection in monolayer MoS<sub>2</sub>/few-layer graphene hybrid spin valves, *Nano Lett.*, 2017, **17**, 3877–3883, DOI: [10.1021/acs.nanolett.7b01393](https://doi.org/10.1021/acs.nanolett.7b01393).
- A. Avsar, D. Unuchek, J. Liu, O. L. Sanchez, K. Watanabe, T. Taniguchi, B. Ozyilmaz and A. Kis, Optospintronics in graphene via proximity coupling, *ACS Nano*, 2017, **11**, 11678–11686, DOI: [10.1021/acsnano.7b06800](https://doi.org/10.1021/acsnano.7b06800).
- T. S. Ghiasi, A. A. Kaverzin, P. J. Blah and B. J. Van Wees, Charge-to-spin conversion by the Rashba–Edelstein effect in two-dimensional van der Waals heterostructures up to room temperature, *Nano Lett.*, 2019, **19**, 5959–5966, DOI: [10.1021/acs.nanolett.9b01611](https://doi.org/10.1021/acs.nanolett.9b01611).
- L. A. Benitez, W. Sávero Torres, J. F. Sierra, M. Timmermans, J. H. Garcia, S. Roche, M. V. Costache and S. O. Valenzuela, Tunable room-temperature spin galvanic and spin Hall effects in van der Waals heterostructures, *Nat. Mater.*, 2020, **19**, 170–175, DOI: [10.1038/s41563-019-0575-1](https://doi.org/10.1038/s41563-019-0575-1).
- F. Zhang, B. Zheng, A. Sebastian, D. H. Olson, M. Liu, K. Fujisawa, Y. T. H. Pham, V. O. Jimenez, V. Kalappattil and L. Miao, others Monolayer vanadium-doped tungsten disulfide: a room-temperature dilute magnetic semiconductor, *Adv. Sci.*, 2020, **7**, 2001174, DOI: [10.1002/advs.202001174](https://doi.org/10.1002/advs.202001174).
- P. M. Coelho, Magnetic doping in transition metal dichalcogenides, *J. Phys.: Condens. Matter*, 2024, **36**, 203001, DOI: [10.1088/1361-648X/ad271b](https://doi.org/10.1088/1361-648X/ad271b).



7 Y. T. H. Pham, M. Liu, V. O. Jimenez, Z. Yu, V. Kalappattil, F. Zhang, K. Wang, T. Williams, M. Terrones and M.-H. Phan, Tunable ferromagnetism and thermally induced spin flip in Vanadium-doped tungsten diselenide monolayers at room temperature, *Adv. Mater.*, 2020, **32**, 2003607, DOI: [10.1002/adma.202003607](https://doi.org/10.1002/adma.202003607).

8 V. Ortiz Jimenez, Y. T. H. Pham, M. Liu, F. Zhang, Z. Yu, V. Kalappattil, B. Muchharla, T. Eggers, D. L. Duong and M. Terrones, others Light-controlled room temperature ferromagnetism in vanadium-doped tungsten disulfide semiconducting monolayers, *Adv. Electron. Mater.*, 2021, **7**, 2100030, DOI: [10.1002/aelm.202100030](https://doi.org/10.1002/aelm.202100030).

9 S. J. Yun, D. L. Duong, D. M. Ha, K. Singh, T. L. Phan, W. Choi, Y.-M. Kim and Y. H. Lee, Ferromagnetic order at room temperature in monolayer WSe<sub>2</sub> semiconductor via vanadium dopant, *Adv. Sci.*, 2020, **7**, 1903076, DOI: [10.1002/advs.201903076](https://doi.org/10.1002/advs.201903076).

10 L.-A. T. Nguyen, J. Jiang, T. D. Nguyen, P. Kim, M.-K. Joo, D. L. Duong and Y. H. Lee, Electrically tunable magnetic fluctuations in multilayered vanadium-doped tungsten diselenide, *Nat. Electron.*, 2023, **6**, 582–589, DOI: [10.1038/s41928-023-01002-1](https://doi.org/10.1038/s41928-023-01002-1).

11 J. Zhang, Y. Zhu, M. Tebyetekerwa, D. Li, D. Liu, W. Lei, L. Wang, Y. Zhang and Y. Lu, Vanadium-doped monolayer MoS<sub>2</sub> with tunable optical properties for field-effect transistors, *ACS Appl. Nano Mater.*, 2020, **4**, 769–777, DOI: [10.1021/acsanm.0c03083](https://doi.org/10.1021/acsanm.0c03083).

12 K. R. Sahoo, J. J. Panda, S. Bawari, R. Sharma, D. Maity, A. Lal, R. Arenal, G. Rajalakshmi and T. N. Narayanan, Enhanced room-temperature spin-valley coupling in V-doped MoS<sub>2</sub>, *Phys. Rev. Mater.*, 2022, **6**, 085202, DOI: [10.1103/PhysRevMaterials.6.085202](https://doi.org/10.1103/PhysRevMaterials.6.085202).

13 D. Maity, R. Sharma, K. R. Sahoo, A. Lal, R. Arenal and T. N. Narayanan, Tuning the electronic structure of monolayer MoS<sub>2</sub> towards metal like via vanadium doping, *Phys. Rev. Mater.*, 2024, **8**, 084002, DOI: [10.1103/PhysRevMaterials.8.084002](https://doi.org/10.1103/PhysRevMaterials.8.084002).

14 D. Zhou, Y. T. H. Pham, D. T.-X. Dang, D. Sanchez, A. Oberoi, K. Wang, A. Fest, A. Sredenscheck, M. Liu, H. Terrones, S. Das, D.-N. Le, L. M. Woods, M.-H. Phan and M. Terrones, Vanadium-doped molybdenum disulfide monolayers with tunable electronic and magnetic properties: do vanadium-vacancy pairs matter?, *arXiv*, 2024, preprint, arXiv:2401.16806, DOI: [10.48550/arXiv.2401.16806](https://doi.org/10.48550/arXiv.2401.16806).

15 Q. Tan, Q. Wang, Y. Liu, C. Liu, X. Feng and D. Yu, Enhanced magnetic properties and tunable Dirac point of graphene/Mn-doped monolayer MoS<sub>2</sub> heterostructures, *J. Phys.: Condens. Matter*, 2018, **30**, 305304, DOI: [10.1088/1361-648X/aacca2](https://doi.org/10.1088/1361-648X/aacca2).

16 L. Cai, H. Duan, Q. Liu, C. Wang, H. Tan, W. Hu, F. Hu, Z. Sun and W. Yan, Ultrahigh-temperature ferromagnetism in MoS<sub>2</sub> Moiré superlattice/graphene hybrid heterostructures, *Nano Res.*, 2021, **14**, 4182–4187, DOI: [10.1007/s12274-021-3360-9](https://doi.org/10.1007/s12274-021-3360-9).

17 E. Nakhmedov, E. Nadimi, S. Vedaei, O. Alekperov, F. Tatardar, A. Najafov, I. Abbasov and A. Saletsky, Vacancy mediated magnetization and healing of a graphene monolayer, *Phys. Rev. B*, 2019, **99**, 125125, DOI: [10.1103/PhysRevB.99.125125](https://doi.org/10.1103/PhysRevB.99.125125).

18 S. K. Tiwari, S. K. Pandey, R. Pandey, N. Wang, M. Bystrzejewski, Y. K. Mishra and Y. Zhu, Stone–wales defect in graphene, *Small*, 2023, **19**, 2303340, DOI: [10.1002/smll.202303340](https://doi.org/10.1002/smll.202303340).

19 Z. Lin, B. R. Carvalho, E. Kahn, R. Lv, R. Rao, H. Terrones, M. A. Pimenta and M. Terrones, Defect engineering of two-dimensional transition metal dichalcogenides, *2D Mater.*, 2016, **3**, 022002, DOI: [10.1088/2053-1583/3/2/022002](https://doi.org/10.1088/2053-1583/3/2/022002).

20 X. Han, M. Niu, Y. Luo, R. Li, J. Dan, Y. Hong, X. Wu, A. V. Trukhanov, W. Ji and Y. Wang, Others Atomically engineering metal vacancies in monolayer transition metal dichalcogenides, *Nat. Synth.*, 2024, **3**, 586–594, DOI: [10.1038/s44160-024-00501-z](https://doi.org/10.1038/s44160-024-00501-z).

21 M. Khan, M. Erementchouk, J. Hendrickson and M. N. Leuenberger, Electronic and optical properties of vacancy defects in single-layer transition metal dichalcogenides, *Phys. Rev. B*, 2017, **95**, 245435, DOI: [10.1103/PhysRevB.95.245435](https://doi.org/10.1103/PhysRevB.95.245435).

22 A. A. Koós, P. Vancsó, M. Szendrő, G. Dobrik, D. Antognini Silva, Z. I. Popov, P. B. Sorokin, L. Henrard, C. Hwang and L. P. Biró, others Influence of native defects on the electronic and magnetic properties of CVD grown MoSe<sub>2</sub> single layers, *J. Phys. Chem. C*, 2019, **123**, 24855–24864, DOI: [10.1021/acs.jpcc.9b05921](https://doi.org/10.1021/acs.jpcc.9b05921).

23 W. S. Yun and J. D. Lee, Strain-induced magnetism in single-layer MoS<sub>2</sub>: origin and manipulation, *J. Phys. Chem. C*, 2015, **119**, 2822–2827, DOI: [10.1021/jp510308a](https://doi.org/10.1021/jp510308a).

24 D. T.-X. Dang, D.-N. Le and L. M. Woods, Dissecting van der Waals interactions with Density Functional Theory–Wannier-basis approach, *Comput. Phys. Commun.*, 2025, 109525, DOI: [10.1016/j.cpc.2025.109525](https://doi.org/10.1016/j.cpc.2025.109525).

25 Y. Wang, S. Li and J. Yi, Electronic and magnetic properties of Co doped MoS<sub>2</sub> monolayer, *Sci. Rep.*, 2016, **6**, 24153, DOI: [10.1038/srep24153](https://doi.org/10.1038/srep24153).

26 W. Hu, H. Tan, H. Duan, G. Li, N. Li, Q. Ji, Y. Lu, Y. Wang, Z. Sun, F. Hu, C. Wang and W. Yan, Synergetic effect of substitutional dopants and sulfur vacancy in modulating the ferromagnetism of MoS<sub>2</sub> nanosheets, *ACS Appl. Mater. Interfaces*, 2019, **11**, 31155–31161, DOI: [10.1021/acsami.9b09165](https://doi.org/10.1021/acsami.9b09165).

27 E. H. Lieb, Two theorems on the Hubbard model, *Phys. Rev. Lett.*, 1989, **62**, 1201, DOI: [10.1103/PhysRevLett.62.1201](https://doi.org/10.1103/PhysRevLett.62.1201).

28 O. V. Yazyev and L. Helm, Defect-induced magnetism in graphene, *Phys. Rev. B: Condens. Matter Mater. Phys.*, 2007, **75**, 125408, DOI: [10.1103/PhysRevB.75.125408](https://doi.org/10.1103/PhysRevB.75.125408).

29 D. Thi-Xuan Dang, R. K. Barik, M.-H. Phan and L. M. Woods, Enhanced magnetism in heterostructures with transition-metal dichalcogenide monolayers, *J. Phys. Chem. Lett.*, 2022, **13**, 8879–8887, DOI: [10.1021/acs.jpclett.2c01925](https://doi.org/10.1021/acs.jpclett.2c01925).

30 C.-M. Hung, D. T.-X. Dang, A. Chanda, D. Detellem, N. Alzahrani, N. Kapuruge, Y. T. H. Pham, M. Liu, D. Zhou, H. R. Gutierrez, D. A. Arena, M. Terrones, S. Witanachchi, L. M. Woods, H. Srikanth and M.-H. Phan, Enhanced magnetism and anomalous Hall transport through two-dimensional tungsten disulfide interfaces, *Nanomaterials*, 2023, **13**, 771, DOI: [10.3390/nano13040771](https://doi.org/10.3390/nano13040771).



31 D. Pierucci, H. Henck, J. Avila, A. Balan, C. H. Naylor, G. Patriarche, Y. J. Dappe, M. G. Silly, F. Sirotti, A. T. C. Johnson, M. C. Asensio and A. Ouerghi, Band alignment and minigaps in monolayer MoS<sub>2</sub>-Graphene van der Waals heterostructures, *Nano Lett.*, 2016, **16**, 4054–4061, DOI: [10.1021/acs.nanolett.6b00609](https://doi.org/10.1021/acs.nanolett.6b00609).

32 B. Chitara, E. Dimitrov, M. Liu, T. R. Seling, B. S. Kolli, D. Zhou, Z. Yu, A. K. Shringi, M. Terrones and F. Yan, Charge transfer modulation in Vanadium-doped WS<sub>2</sub>/Bi<sub>2</sub>O<sub>2</sub>Se heterostructures, *Small*, 2023, **19**, 2302289, DOI: [10.1002/smll.202302289](https://doi.org/10.1002/smll.202302289).

33 L. Cai, J. He, Q. Liu, T. Yao, L. Chen, W. Yan, F. Hu, Y. Jiang, Y. Zhao, T. Hu, Z. Sun and S. Wei, Vacancy-induced ferromagnetism of MoS<sub>2</sub> nanosheets, *J. Am. Chem. Soc.*, 2015, **137**, 2622–2627, DOI: [10.1021/ja5120908](https://doi.org/10.1021/ja5120908).

34 A. k. Anbalagan, *et al.*, Gamma-ray irradiation induced ultrahigh room-temperature ferromagnetism in MoS<sub>2</sub> sputtered few-layered thin films, *ACS Nano*, 2023, **17**, 6555–6564, DOI: [10.1021/acsnano.2c11955](https://doi.org/10.1021/acsnano.2c11955).

35 C. K. Safeer, J. Inglá-Aynés, F. Herling, J. H. Garcia, M. Vila, N. Ontoso, M. R. Calvo, S. Roche, L. E. Hueso and F. Casanova, Room-temperature spin hall effect in graphene/MoS<sub>2</sub> van der waals heterostructures, *Nano Lett.*, 2019, **19**, 1074–1082, DOI: [10.1021/acs.nanolett.8b04368](https://doi.org/10.1021/acs.nanolett.8b04368).

36 L. Yu, Y.-H. Lee, X. Ling, E. J. G. Santos, Y. C. Shin, Y. Lin, M. Dubey, E. Kaxiras, J. Kong, H. Wang and T. Palacios, Graphene/MoS<sub>2</sub> hybrid technology for large-scale two-dimensional electronics, *Nano Lett.*, 2014, **14**, 3055–3063, DOI: [10.1021/nl404795z](https://doi.org/10.1021/nl404795z).

37 G. Kresse and J. Furthmüller, Efficient iterative schemes for ab initio total-energy calculations using a plane-wave basis set, *Phys. Rev. B: Condens. Matter Mater. Phys.*, 1996, **54**, 11169, DOI: [10.1103/PhysRevB.54.11169](https://doi.org/10.1103/PhysRevB.54.11169).

38 P. Hohenberg and W. Kohn, Inhomogeneous electron gas, *Phys. Rev.*, 1964, **136**, B864, DOI: [10.1103/PhysRev.136.B864](https://doi.org/10.1103/PhysRev.136.B864).

39 G. Kresse and D. Joubert, From ultrasoft pseudopotentials to the projector augmentedwave method, *Phys. Rev. B: Condens. Matter Mater. Phys.*, 1999, **59**, 1758, DOI: [10.1103/PhysRevB.59.1758](https://doi.org/10.1103/PhysRevB.59.1758).

40 J. P. Perdew, K. Burke and M. Ernzerhof, Generalized gradient approximation made simple, *Phys. Rev. Lett.*, 1996, **77**, 3865, DOI: [10.1103/PhysRevLett.77.3865](https://doi.org/10.1103/PhysRevLett.77.3865).

41 S. Grimme, S. Ehrlich and L. Goerigk, Effect of the damping function in dispersion corrected density functional theory, *J. Comput. Chem.*, 2011, **32**, 1456–1465, DOI: [10.1002/jcc.21759](https://doi.org/10.1002/jcc.21759).

42 S. L. Dudarev, G. A. Botton, S. Y. Savrasov, C. Humphreys and A. P. Sutton, Electron energy-loss spectra and the structural stability of nickel oxide: An LSDA+ U study, *Phys. Rev. B: Condens. Matter Mater. Phys.*, 1998, **57**, 1505, DOI: [10.1103/PhysRevB.57.1505](https://doi.org/10.1103/PhysRevB.57.1505).

